

Signal Reconstruction for the MAGIC Telescope

J. Albert ^a, E. Aliu ^b, H. Anderhub ^c, P. Antoranz ^d,
A. Armada ^b, C. Baixeras ^e, J. A. Barrio ^d, H. Bartko ^{g,*},
D. Bastieri ^h, J. Becker ^f, W. Bednarek ^j, K. Berger ^a,
C. Bigongiari ^h, A. Biland ^c, R. K. Bock ^{g,h}, P. Bordas ^v,
V. Bosch-Ramon ^v, T. Bretz ^a, I. Britvitch ^c, M. Camara ^d,
E. Carmona ^g, A. Chilingarian ^k, S. Ciprini ^l, J. A. Coarasa ^g,
S. Commichau ^c, J. L. Contreras ^d, J. Cortina ^b,
M. T. Costado ^m, V. Curtef ^f, V. Danielyan ^k, F. Dazzi ^h,
A. De Angelis ⁱ, R. de los Reyes ^d, B. De Lotto ⁱ,
C. Delgado Mendez ^m, E. Domingo-Santamaría ^b, D. Dorner ^a,
M. Doro ^h, M. Errando ^b, M. Fagiolini ^p, D. Ferenc ^o,
E. Fernández ^b, R. Firpo ^b, J. Flix ^b, M. V. Fonseca ^d, L. Font ^e,
M. Fuchs ^g, N. Galante ^g, R. Garcia Lopez ^m, M. Garzarczyk ^g,
M. Gaug ^{h,*}, M. Giller ^j, F. Goebel ^g, D. Hakobyan ^k,
M. Hayashida ^g, T. Hengstebeck ⁿ, A. Herrero ^m, D. Höhne ^a,
J. Hose ^g, C. C. Hsu ^g, P. Jacon ^j, T. Jogler ^g, O. Kalekin ⁿ,
R. Kosyra ^g, D. Kranich ^c, R. Kritzer ^a, A. Laille ^o, P. Liebing ^g,
E. Lindfors ^l, S. Lombardi ^h, F. Longo ^q, J. López ^b, M. López ^d,
E. Lorenz ^{c,g}, P. Majumdar ^g, G. Maneva ^r, K. Mannheim ^a,
O. Mansutti ⁱ, M. Mariotti ^h, M. Martínez ^b, D. Mazin ^g,
C. Merck ^g, M. Meucci ^p, M. Meyer ^a, J. M. Miranda ^d,
R. Mirzoyan ^g, S. Mizobuchi ^g, A. Moralejo ^b, K. Nilsson ^l,
J. Ninkovic ^g, E. Oña-Wilhelmi ^b, N. Otte ^g, I. Oya ^d,
D. Paneque ^g, M. Panniello ^m, R. Paoletti ^p, J. M. Paredes ^v,
M. Pasanen ^l, D. Pascoli ^h, F. Pauss ^c, R. Pegna ^p, M. Persic ^s,
L. Peruzzo ^h, A. Piccioli ^p, M. Poller ^a, N. Puchades ^b,
E. Prandini ^h, A. Raymers ^k, W. Rhode ^f, M. Ribó ^v, J. Rico ^b,
M. Rissi ^c, A. Robert ^e, S. Rügamer ^a, A. Saggion ^h, A. Sánchez ^e,
P. Sartori ^h, V. Scalzotto ^h, V. Scapin ^h, R. Schmitt ^a,
T. Schweizer ⁿ, M. Shayduk ⁿ, K. Shinozaki ^g, S. N. Shore ^t,

N. Sidro ^b, A. Sillanpää ^ℓ, D. Sobczynska ^j, A. Stamerra ^p,
L. S. Stark ^c, L. Takalo ^ℓ, P. Temnikov ^r, D. Tescaro ^b,
M. Teshima ^g, N. Tonello ^g, D. F. Torres ^{b,u}, N. Turini ^p,
H. Vankov ^r, V. Vitale ⁱ, R. M. Wagner ^g, T. Wibig ^j,
W. Wittek ^g, R. Zanin ^h, J. Zapatero ^e

^a*Universität Würzburg, D-97074 Würzburg, Germany*

^b*Institut de Física d'Altes Energies, Edifici Cn., E-08193 Bellaterra (Barcelona), Spain*

^c*ETH Zurich, CH-8093 Switzerland*

^d*Universidad Complutense, E-28040 Madrid, Spain*

^e*Universitat Autònoma de Barcelona, E-08193 Bellaterra, Spain*

^f*Universität Dortmund, D-44227 Dortmund, Germany*

^g*Max-Planck-Institut für Physik, D-80805 München, Germany*

^h*Università di Padova and INFN, I-35131 Padova, Italy*

ⁱ*Università di Udine, and INFN Trieste, I-33100 Udine, Italy*

^j*University of Łódź, PL-90236 Lodz, Poland*

^k*Yerevan Physics Institute, AM-375036 Yerevan, Armenia*

^ℓ*Tuorla Observatory, FI-21500 Piikkiö, Finland*

^m*Instituto de Astrofísica de Canarias, E-38200, La Laguna, Tenerife, Spain*

ⁿ*Humboldt-Universität zu Berlin, D-12489 Berlin, Germany*

^o*University of California, Davis, CA-95616-8677, USA*

^p*Università di Siena, and INFN Pisa, I-53100 Siena, Italy*

^q*Università di Trieste, and INFN Trieste, I-34100 Trieste, Italy*

^r*Institute for Nuclear Research and Nuclear Energy, BG-1784 Sofia, Bulgaria*

^s*INAF/Osservatorio Astronomico and INFN Trieste, I-34131 Trieste, Italy*

^t*Università di Pisa, and INFN Pisa, I-56126 Pisa, Italy*

^u*ICREA and Institut de Ciències de l'Espai, IEEC-CSIC, E-08193 Bellaterra, Spain*

^v*Universitat de Barcelona, E-08028 Barcelona, Spain*

Abstract

The MAGIC telescope uses a 300 MHz FADC system to sample the shaped PMT signals produced by the captured Cherenkov photons of air showers. Different algorithms to reconstruct the signal from the read-out samples (extractors) have been developed and are described and compared. Criteria based on the obtained charge and time resolution/bias are defined and used to judge the different extractors, by

applying them to calibration, cosmic and pedestal signals. The achievable charge and time resolution have been derived as a function of the incident number of photo-electrons.

Key words: fast digitization, FADC, digital filter, Cherenkov imaging telescopes, gamma-ray astronomy.

1 Introduction

The Major Atmospheric Gamma ray Imaging Cherenkov (MAGIC) telescope [1–3] aims at studying the very high energy (VHE, $E > 50$ GeV) γ -ray emission from astrophysical sources at the lowest possible energy threshold using the IACT technique [4, 5]: A VHE γ -ray entering the earth’s atmosphere initiates a shower of electrons and positrons with a particle density maximum about 10 km above sea level (for an energy of 1 TeV). The particles in the cascade produce Cherenkov light in a cone of about 1° half-angle which illuminates an area of around 120 m radius on the ground. In case the MAGIC telescope lies within this illuminated area, it collects part of the Cherenkov light with its mirrors and projects a shower image onto the photomultiplier tube (PMT) camera. The Cherenkov photons arrive within a very short time interval of a few nanoseconds at the telescope camera, whose pixels are fast light sensors such as PMTs, so that one can trigger on the coincident light signals. The fluctuations of the light of the night sky (LONS) cause background noise. This effect is minimized by using low exposure times (signal integration times), typically of the order of ten nanoseconds.

Figure 1 shows a MC simulated pulse (black line) and the simulated FADC slices (blue points) for a typical MC γ -ray event after pedestal subtraction. From the FADC slices two quantities of interest shall be reconstructed:

- (1) **Signal Charge:** The total signal charge (the total number of photo electrons released from the photocathode of the PMT) is proportional to the total area below the pulse. The sum of the signal charges of all camera pixels is a measure of the shower energy.
- (2) **Signal Arrival time:** The time difference between the first recorded FADC sample and a characteristic position on the pulse shape, like the maximum, the half-maximum on the rising edge or the center of gravity of the pulse.

* Corresponding author.

Email addresses: hbartko@mppmu.mpg.de (H. Bartko), gaug@pd.infn.it (M. Gaug).

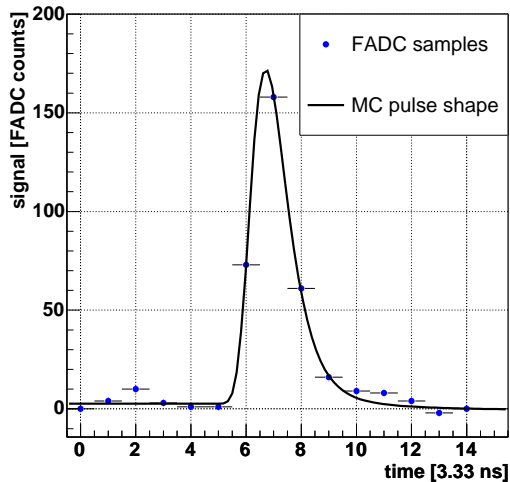


Fig. 1. Simulated signal pulse shape (black line) and FADC slices (blue points) for a typical MC event. The FADC measurements are affected by noise, e.g. at $t=2 \times 3.33\text{ns}$ there is a noise peak due to LONS. The total signal charge corresponds to the area below the black curve and the signal arrival time is the time difference between the first FADC sample and a characteristic position on the pulse shape, like the maximum, the half-maximum on the rising edge or the center of gravity of the pulse.

To reach the highest sensitivity and the lowest energy threshold, the recorded signals have to be accurately reconstructed. Therefore the highest possible signal-to-noise ratio and signal charge/time resolution, as well as a small bias are important.

The main background originates from the much more frequent showers induced by isotropic hadronic cosmic rays. Monte Carlo (MC) based simulations predict different time structures for γ -ray and hadron induced shower images as well as for images of single muons [6]. An accurate arrival time determination may therefore improve the γ /hadron separation power. Moreover, the timing information may be used to discriminate between pixels whose signal belongs to the shower and pixels which are affected by randomly timed background noise. The pixels with a low signal-to-noise ratio are rejected for the subsequent image parameterization [7, 8].

This paper is structured as follows: In section 2 the read-out system of the MAGIC telescope is described and in section 3 the average pulse shapes of calibration and cosmic pulses are reconstructed from the recorded FADC samples. These pulse shapes are compared to that implemented in the MC simulation program. In section 4 criteria for an optimal signal reconstruction are developed. In section 5 the signal reconstruction algorithms as well as their implementation in the MAGIC software framework (**MARS** [10]) are described. Thereafter, the performance of the signal extraction algorithms under study is

assessed by applying them to pedestal, calibration and MC events (sections 6 to 8). Section 9 states the CPU time requirements for the different signal reconstruction algorithms. Finally in section 10 the results are summarized and in section 11 an outlook is given.

2 Signal read-out

Figure 2 shows a sketch of the MAGIC read-out system, including the PMT camera, the analog-optical link, the majority trigger logic and flash analog-to-digital converters (FADCs). The used PMTs (ET 9116A from Electron Tubes) provide a very fast response to the input light signal. The response of the PMTs to sub-ns input light pulses shows a full width at half maximum (FWHM) of 1.0 - 1.2 ns and rise and fall times of 600 and 700 ps correspondingly [11]. A transmitter, which uses a vertical-cavity surface-emitting laser (VCSEL) diode modulated in amplitude, converts the electrical pulse supplied by the PMT into an optical one. This signal is then transferred via 162 m long, 50/125 μm diameter optical fibers to the counting house [12]. After transforming the light back to an electrical signal, the original PMT pulse has a FWHM of about 2.2 ns for a single photo-electron pulse and rise and fall times of about 1 ns.

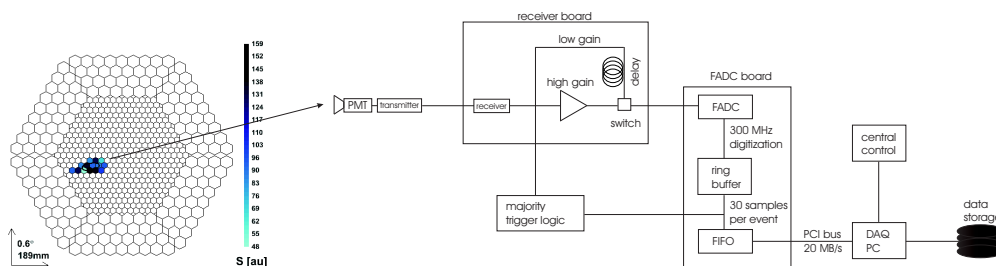


Fig. 2. MAGIC read-out scheme: the analog PMT signals are transferred via an analog optical link to the counting house where – after the trigger decision – the signals are digitized by a 300 MHz FADCs system and written to the hard disk of a data acquisition PC.

In order to sample this pulse shape with the 300 MSamples/s FADC system, the original pulse is folded with a stretching function of 6 ns, leading to a FWHM greater than 6 ns. In order to increase the dynamic range of the read-out, the signals are split into two branches with gains differing by a factor 10. One branch is delayed by 55 ns and then both branches are multiplexed and read-out by one FADC. Figure 3 shows a typical pulse (generated by a fast pulser, see section 3) as measured by one FADC. A more detailed overview about the MAGIC read-out and DAQ system can be found in [13]. Planned upgrades of the read-out system to a higher sampling speed are described in [14, 15].

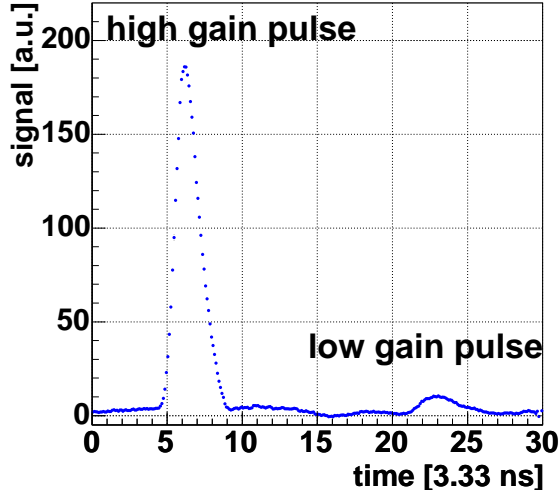


Fig. 3. Average reconstructed pulse shape from a fast pulse generator showing the high gain and the low gain pulse. The FWHM of the high gain pulse is about 6.3 ns while the FWHM of the low gain pulse is about 10 ns.

The following intrinsic characteristics of the current read-out system affect especially the signal reconstruction:

Inner and Outer pixels: The MAGIC camera has two types of pixels filling, respectively, the inner and the outer parts of the camera (see Figure 2), with the following differences:

- (1) Size: The outer pixels have a factor four bigger area than the inner pixels [16]. Their (quantum-efficiency convoluted) effective area is about a factor 2.6 higher.
- (2) Gain: The camera is flat-fielded in order to yield a similar reconstructed charge signal in all pixels, for the same photon illumination intensity. In order to achieve this, the gain of the inner pixels has been adjusted to about a factor 2.6 higher than the outer ones [19]. This results in a lower effective noise charge from the night sky background for the outer pixels.
- (3) Delay: Due to the lower high voltage (HV) settings of the outer pixels, their signals are delayed by about 1.5 ns with respect to the inner ones.

Asynchronous trigger: The FADC clock is not synchronized with the trigger. Therefore the time t_{rel} between the trigger decision and the first read-out sample is uniformly distributed along the range $t_{\text{rel}} \in [0, T_{\text{FADC}}]$, where $T_{\text{FADC}} = 3.33$ ns is the digitization period of the MAGIC 300 MHz FADCs.

AC coupling: The PMT signals are AC-coupled at various places in the signal transmission chain. Thus the contribution of the PMT pulses due to the light of the night sky (LONS) is on average zero. Only the signal RMS depends on the intensity of the LONS. In moonless nights, observing an extra-galactic source, an average background rate of about 0.13 photo-electrons per nano-second per inner pixel has been measured [14].

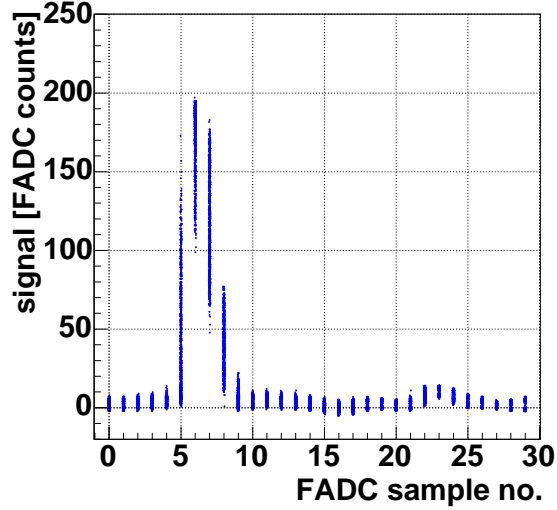


Fig. 4. Superimposed FADC slices of 1000 pulse generator pulses.

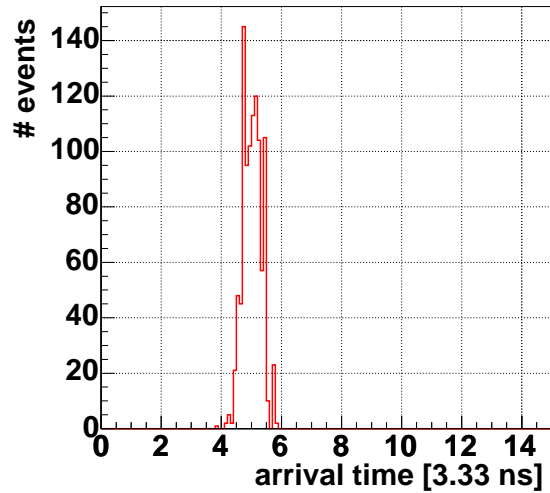


Fig. 5. Distribution of the reconstructed arrival time from the raw FADC samples shown in Figure 4. The distribution has a width of about 1 FADC period (3.33 ns) due to the asynchronous trigger with respect to the FADC clock.

Figure 4 shows the raw FADC values as a function of the slice number for 1000 constant pulse generator pulses overlaid and Figure 5 shows the distribution of the corresponding reconstructed arrival times. The distribution has a width of about 1 FADC period (3.33 ns) due to the asynchronous trigger with respect to the FADC clock.

Shaping: The optical receiver board shapes the pulse with shaping times of about 6 ns, much larger than the typical intrinsic pulse width. Since the shaping time is larger than the width of a single FADC slice, a strong correlation of the noise between neighbouring FADC slices is expected.

Instantaneous amplitudes: The MAGIC FADCs consist of a series of small comparators which measure the momentaneous amplitude of a pulse at a

time. No charge integration over the duration of a time slice is performed by the FADCs. Therefore, pulse structures with a higher frequency than 150 MHz are lost.

3 Pulse Shape

The fact that the signal pulses are sampled asynchronously by the FADCs allows one to determine the average pulse shape with high accuracy. To do that, the signal samples from different recorded pulses are shifted to a common arrival time and normalized to a common area/charge. Therefore, the precision of the determination of each point along the pulse shape depends on the accuracy of the arrival time and charge reconstruction. The relative statistical error of the value of every reconstructed point is well below 10^{-2} . On the other hand, possible biases in the charge and arrival time reconstruction may introduce systematic errors, whose size are unknown at first hand. Figure 3 shows the average signal from a fast pulser as reconstructed by the MAGIC read-out system. The pulser generates unipolar pulses of about 2.5 ns FWHM and preset amplitude. These electrical pulses are fed to the VCSEL transmitters and are transmitted using the same analog-optical link as the PMT pulses and are fed to the MAGIC receiver board. The pulse generator setup is mainly used for test purposes of the receiver board, trigger logic and FADCs.

Figure 6 (left) shows the normalized average pulse shape for the pulse generator in the high and in the low gain, respectively. The intrinsic FWHM of the generated pulses is 2.5 ns, whereas it is on average 6.3 ns and 10 ns for the pulses reconstructed from the high and low gain chains, respectively. The broadening of the low gain pulses with respect to that of the high gain is due to the limited bandwidth of the passive 55 ns on-board delay line of the MAGIC receiver boards.

Figure 6 (right) shows the normalized average reconstructed pulse shapes for green and UV calibration LED pulses [17] (see section 8) as well as that of cosmic events. The shapes of the UV calibration and cosmic pulses are quite similar. Both have a FWHM of about 6.3 ns. Since air showers from hadronic cosmic rays trigger the telescope much more frequently than γ -ray showers, the reconstructed pulse shape of the cosmic events corresponds mainly to hadron induced showers. The pulse shape from electromagnetic air showers might be slightly different as indicated by MC simulations [6, 20]. The pulse shape for green calibration LED pulses is wider and has a pronounced tail.

The reconstructed pulse shapes for generator pulses, cosmic and calibration events allow one to implement a representative pulse shape in the MC simu-

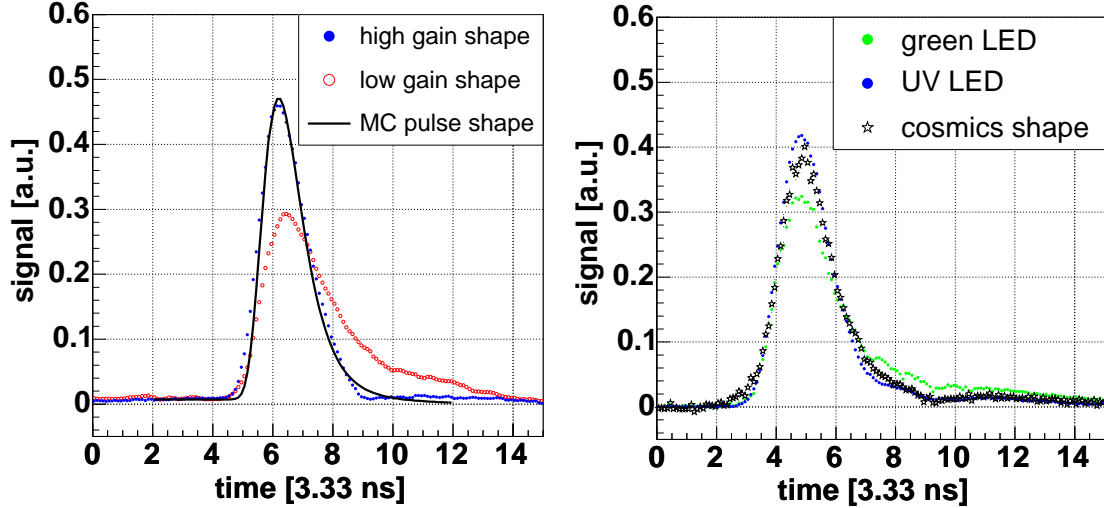


Fig. 6. Left: Average reconstructed high gain and low gain pulse shapes from a pulse generator run. The black line corresponds to the pulse shape implemented into the MC simulations [18]. Right: Average reconstructed high gain pulse shape for calibration runs with green and UV light (see section 8). All histograms/curves are normalized to a common arrival time and area.

lations, see e.g. the full black line in figure 6, left panel. Also the difference between the FWHM of the pulses in the high and the low gain has to be taken into account for the MC simulations and for the signal extraction algorithms. Moreover the shape difference between the calibration pulses and the cosmic pulses has to be corrected for in the calibration procedure [19].

4 Criteria for the Optimal Signal Extraction

The goal of the optimal signal reconstruction algorithm is to compute an unbiased estimate of the charge and arrival time of the Cherenkov pulse with the highest possible resolution. An accurate determination of the arrival time may help distinguish between signal and background. The signal arrival time varies smoothly from pixel to pixel while the background noise is randomly distributed in time.

In the following, a brief introduction to the theory of signal extraction is given and criteria for an optimal signal reconstruction algorithm are developed according to [21].

Let us consider a large number of identical signals, corresponding to a fixed number of photo-electrons N_{phe} . By applying a signal extraction algorithm, a distribution of estimated signals \widehat{N}_{phe} is obtained. The deviation between true and reconstructed value is given by:

$$X = \widehat{N}_{\text{phe}} - N_{\text{phe}} . \quad (1)$$

The distribution of X has a mean B and a variance V defined as:

$$B \equiv \langle X \rangle = \langle \widehat{N}_{\text{phe}} \rangle - N_{\text{phe}} \quad (2)$$

$$V \equiv \langle (X - B)^2 \rangle = \text{Var}[\widehat{N}_{\text{phe}}] \quad (3)$$

$$RMSE \equiv \sqrt{\langle X^2 \rangle} = \sqrt{V + B^2} . \quad (4)$$

The parameter B is also called the **Bias** of the estimator and $RMSE$ is the **Root Mean-Squared Error** which combines resolution and bias. Typically, one measures easily the parameter V , but needs the $RMSE$ for statistical analysis. However, only in case of a vanishing bias, the two numbers are equal.

Generally, both B and $RMSE$ depend on N_{phe} and the background fluctuations BG . In the case of MAGIC the background fluctuations are due to the electronics noise and the PMT response to the LONS. The signals from the latter have the same shape than those from Cherenkov pulses. Therefore, those algorithms which search for the highest sum of a number of consecutive FADC slices inside a global time window (a so-called **sliding window algorithm**) will have a bias. In case of no Cherenkov signal they will typically reconstruct the largest noise pulse. Nevertheless, such a sliding window algorithm usually has a much smaller variance and in many cases a smaller $RMSE$ than the **fixed window extractors**, which just sum up a fixed number of FADC slices. For the description of the signal reconstruction algorithms see section 5.

The reconstructed charge should be proportional to the total number of photoelectrons in the PMT. The linearity is very important for the reconstruction of the shower energy and hence for the measurement of energy spectra from astronomical sources. A deviation from linearity is usually obtained in the following cases:

- At very low signals, the bias causes too high a signal to be reconstructed (positive X).
- At very high signals, the FADC system goes into saturation and the reconstructed signal becomes too low (negative X).
- Any error in the inter-calibration between the high and low gain acquisition channels yields an effective deviation from linearity.

Another important feature of an extractor is its robustness, i.e. its stability in reconstructing the charge and arrival time for different types of pulses with different intrinsic shapes and background levels:

- Cherenkov signals from γ -rays, hadrons and muons
- calibration pulses from different LED color pulsers
- pulse generator pulses.

Finally, the extractor has to accurately reconstruct the high and low gain channels. Due to the analog delay line, the low gain pulse is wider and the charge spans a longer time window. The time delay between the tail of the high gain pulse and the rising edge of the low gain pulse is small. Thus for large pulses, mis-interpretations between the tail of the high gain pulse and the low gain pulse might occur. Moreover, the total recorded time window is relatively small such that parts of the low gain pulse might already lay out of the recorded FADC window. A good extractor must stably extract the low gain pulse without being confused by the above issues.

5 Signal Reconstruction Algorithms

We have chosen four algorithms for the study of the reconstruction of the signal charge and arrival time, namely:

- Fixed Window
- Sliding Window with Amplitude-weighted Time
- Cubic Spline with Integral or Amplitude Extraction
- Digital Filter.

5.1 *Fixed Window*

This signal extraction algorithm simply adds the pedestal-subtracted FADC slice contents of a fixed range (window) of consecutive FADC slices. The window has to be chosen large enough to always cover the complete pulse, otherwise physical differences in the pulse position with respect to the FADC slice numbering would lead to integration of different parts of the pulse. For this reason, the fixed window algorithm adds up more noise than the other considered signal reconstruction algorithms. Due to the AC-coupling of the read-out chain, the reconstructed signals have no bias.

In the current implementation, the fixed window algorithm does not calculate arrival times.

5.2 Sliding Window with Amplitude-weighted Time

This signal extraction algorithm searches for the maximum integral content among all possible FADC windows of fixed size contained in a defined time range (global window). The arrival time is calculated from the window with the highest integral as:

$$t = \frac{\sum_{i=i_0}^{i_0+ws-1} s_i \cdot t_i}{\sum_{i=i_0}^{i_0+ws-1} s_i}, \quad (5)$$

where i denotes the FADC slice index, starting from slice i_0 and running over a window of size ws . The s_i are the pedestal-subtracted FADC slice contents and the t_i are the corresponding times relative to the first recorded FADC slice.

5.3 Cubic Spline with Integral or Amplitude Extraction

This signal extraction algorithm interpolates the pedestal-subtracted FADC slice contents using a cubic spline algorithm, adapted from [22]. In a second step, it searches for the position of the maximum of the interpolation function. Thereafter, two different estimators of the pulse charge are available, namely:

- (1) **Amplitude:** the value of the spline maximum is taken as reconstructed signal.
- (2) **Integral:** The interpolation function is integrated in a window of fixed size, with integration limits determined with respect to the position of the spline maximum.

The pulse arrival times can also be estimated in two ways:

- (1) **Pulse maximum:** The position of the spline maximum determines the arrival time.
- (2) **Pulse Half Maximum:** The position of the half maximum at the rising edge of the pulse determines the arrival time.

5.4 Digital Filter

The goal of the digital filtering method [23, 24] is to optimally reconstruct the charge and arrival time of a signal whose shape is known. Thereby, the noise

contributions to the amplitude and arrival time reconstruction are minimized, see also [26].

For the digital filtering method to work properly, two conditions have to be fulfilled:

- The normalized signal shape has to be constant.
- The noise properties must be constant, i.e. the noise is stationary and independent of the signal amplitude.

As the pulse shape is mainly determined by the artificial pulse stretching on the optical receiver board, the first assumption holds to a good approximation for all pulses with intrinsic signal widths much smaller than the shaping constant. Also the second assumption is fulfilled to a good approximation: Signal and noise are independent and the measured pulse is a linear superposition of the signal and noise contributions.

Let $g(t)$ be the normalized signal shape (e.g. from Figure 6), E the signal integral (charge) and τ the shift between the timing of the physical and the considered/probed signals. Then the time dependence of the signal is given by $y(t) = E \cdot g(t - \tau) + b(t)$, where $b(t)$ is the time-dependent noise contribution. For small time shifts τ the time dependence can be linearized. Discrete measurements y_i of the signal at times t_i ($i = 1, \dots, n$) have the form $y_i = E \cdot g_i - E\tau \cdot \dot{g}_i + O(\tau^2) + b_i$, where $\dot{g}(t)$ is the time derivative of the signal shape, $g_i = g(t_i)$ and $b_i = b(t_i)$.

The correlation of the noise contributions at times t_i and t_j can be expressed by the noise autocorrelation matrix

$$\mathbf{B} : B_{ij} = \langle b_i b_j \rangle - \langle b_i \rangle \langle b_j \rangle , \quad (6)$$

whose elements can be obtained from pedestal data (see section 7). Figure 7 shows the measured noise autocorrelation matrix for different LONS levels. It is dominated by LONS pulses shaped to about 6.5 ns FWHM. The noise auto-correlation in the low gain channel cannot be determined from data. The low gain channel read-out is only activated in case the high gain signal is above a certain threshold resulting in a measurable low gain signal. It has to be retrieved from Monte-Carlo studies instead.

For a given pulse, E and $E\tau$ can be estimated from the n FADC measurements $\mathbf{y} = (y_1, \dots, y_n)$ by minimizing the deviation between the measured and the known pulse shape, and taking into account the known noise auto-correlation, i.e. minimizing the following expression (in matrix form):

$$\chi^2(E, E\tau) = (\mathbf{y} - E\mathbf{g} - E\tau\dot{\mathbf{g}})^T \mathbf{B}^{-1} (\mathbf{y} - E\mathbf{g} - E\tau\dot{\mathbf{g}}) + O(\tau^2) . \quad (7)$$

This leads to the following solution:

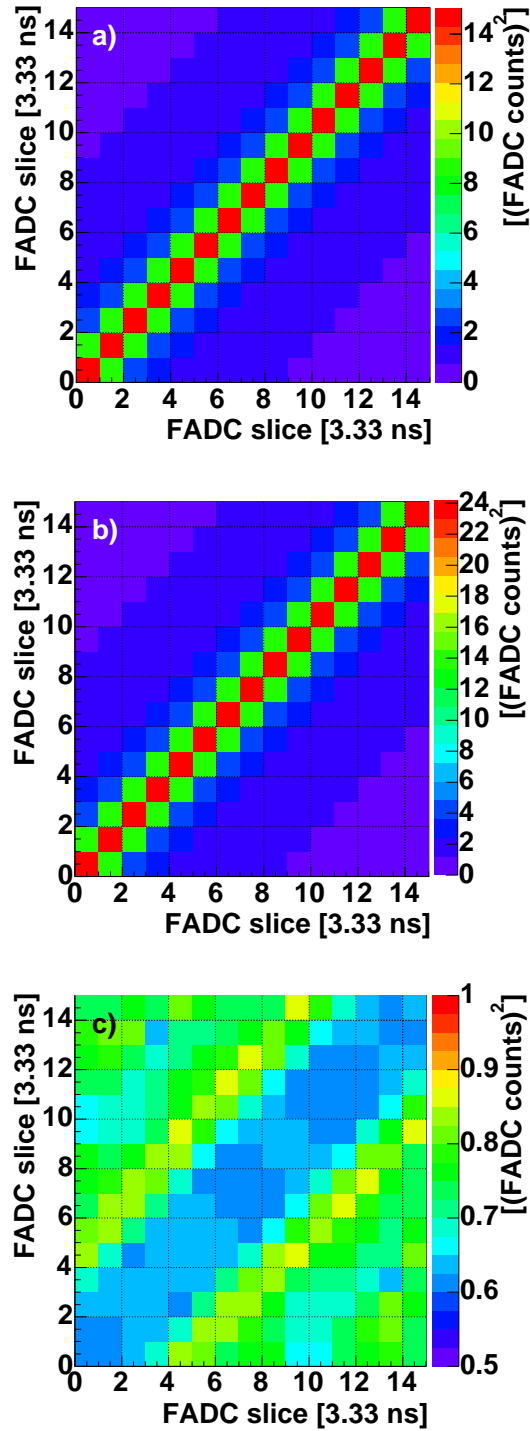


Fig. 7. a,b) Noise autocorrelation matrix B averaged over all pixels for two different LONS levels: a) telescope pointing off the galactic plane, b) telescope pointing into the galactic plane. c) The ratio between a) and b). One can see that the entries of B do not simply scale with the amount of night sky background.

$$E = \mathbf{w}_{\text{amp}}^T(t_{\text{rel}})\mathbf{y} + O(\tau^2) \quad , \quad \mathbf{w}_{\text{amp}}(t_{\text{rel}}) = \frac{(\dot{\mathbf{g}}^T \mathbf{B}^{-1} \dot{\mathbf{g}}) \mathbf{B}^{-1} \mathbf{g} - (\mathbf{g}^T \mathbf{B}^{-1} \dot{\mathbf{g}}) \mathbf{B}^{-1} \dot{\mathbf{g}}}{(\mathbf{g}^T \mathbf{B}^{-1} \mathbf{g})(\dot{\mathbf{g}}^T \mathbf{B}^{-1} \dot{\mathbf{g}}) - (\mathbf{g}^T \mathbf{B}^{-1} \dot{\mathbf{g}})^2} \quad , \quad (8)$$

$$E\tau = \mathbf{w}_{\text{time}}^T(t_{\text{rel}})\mathbf{y} + O(\tau^2) \quad , \quad \mathbf{w}_{\text{time}}(t_{\text{rel}}) = \frac{(\mathbf{g}^T \mathbf{B}^{-1} \mathbf{g}) \mathbf{B}^{-1} \dot{\mathbf{g}} - (\mathbf{g}^T \mathbf{B}^{-1} \dot{\mathbf{g}}) \mathbf{B}^{-1} \mathbf{g}}{(\mathbf{g}^T \mathbf{B}^{-1} \mathbf{g})(\dot{\mathbf{g}}^T \mathbf{B}^{-1} \dot{\mathbf{g}}) - (\mathbf{g}^T \mathbf{B}^{-1} \dot{\mathbf{g}})^2} \quad , \quad (9)$$

where t_{rel} is the time difference between the trigger decision and the first read-out sample, see section 3. Thus E and $E\tau$ are given by a weighted sum of the discrete measurements y_i with the weights for the amplitude, $w_{\text{amp}}(t_{\text{rel}})$, and time shift, $w_{\text{time}}(t_{\text{rel}})$, plus $O(\tau^2)$. To reduce $O(\tau^2)$ the fit can be iterated using $g(t_1 = t - \tau)$ and the weights $w_{\text{amp/time}}(t_{\text{rel}} + \tau)$ [23]. Figure 8 shows examples of digital filter weights. The result for E and $E\tau$ is independent of the number n of FADC measurement used.

The expected contributions of the noise to the error of the estimated amplitude and timing only depend on the the shape $g(t)$, and the noise auto-correlation \mathbf{B} . The corresponding analytic expressions can be found in [23].

6 Monte Carlo Studies

Some characteristics of the extractor can only be investigated with the use of Monte-Carlo simulations of signal pulses and noise (for the MAGIC MC simulations, see reference [18]). While in real conditions the charge of the pulse for a given number of incoming Cherenkov photons is Poisson distributed due to the PMT photo-electron statistics, simulated pulses of a specific number of photo-electrons can be generated. Moreover, using MC, the same pulse can be studied with and without added noise, where the noise level can be deliberately adjusted. In the subsequent studies, the Monte Carlo simulation was used to determine, for each of the tested extractors, the following quantities:

- The bias as a function of the input signal charge.
- The charge resolution as a function of the input signal charge.
- The time resolution as a function of the input signal charge.
- The effect of adding or removing noise to the above quantities.

The following settings have been used:

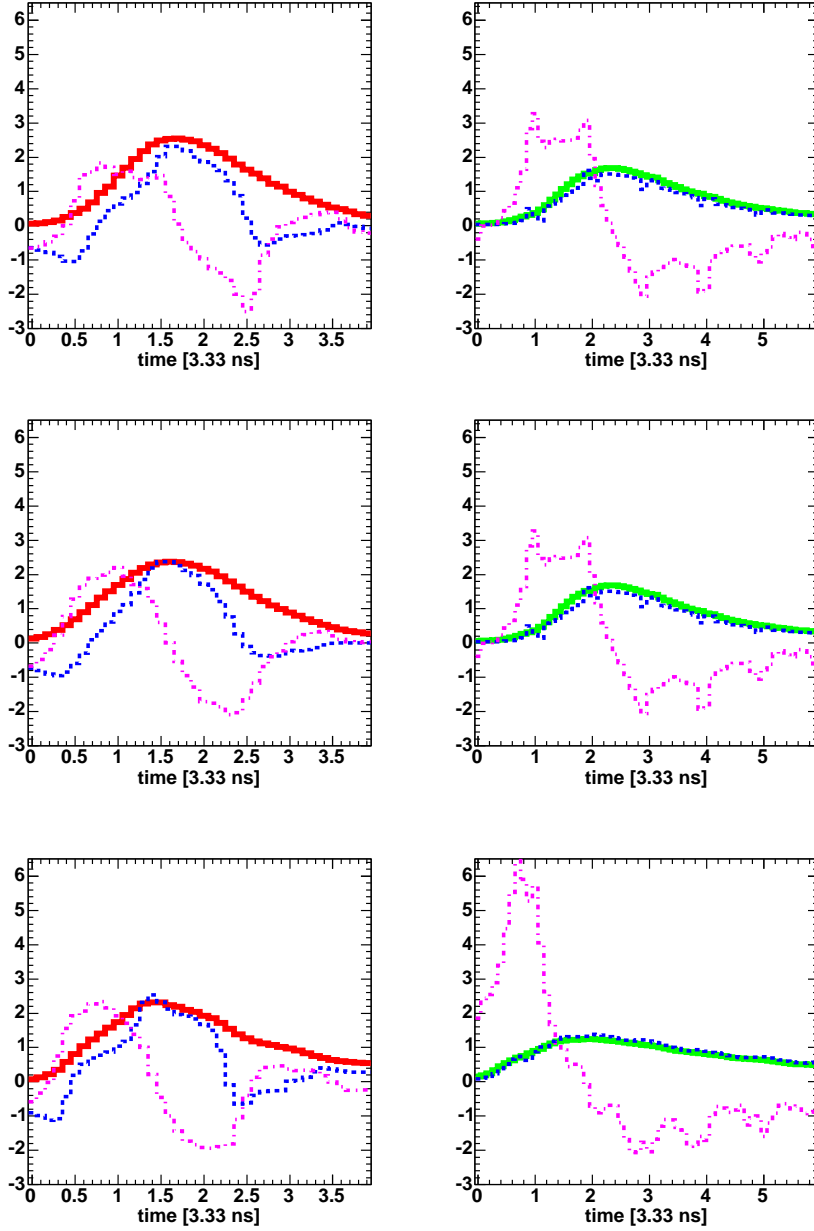


Fig. 8. Examples of digital filter weights. Top: cosmic pulses, center: UV calibration pulses and bottom: blue and green calibration pulses. On the left side, the high gain pulse is shown, on the right side, the low gain. Full lines show the normalized signal shapes $g(t)$ (multiplied by 5 for better visibility), dashed lines the amplitude weights $w_{\text{amp}}(t)$, and dotted-dashed lines the time weights $w_{\text{time}}(t)$. For the high-gain extraction 4 FADC slices are used and for the low-gain extraction 6 FADC slices.

- The conversion factor from photo-electrons to integrated charge over the whole pulse was set to 7.8 FADC counts per photo-electron.
- The relative timing between the trigger and the signal pulse was uniformly distributed over 1 FADC slice.
- The LONS has been simulated approximately as in extra-galactic source observation conditions.
- The electronics noise has been simulated Gaussian at the level measured in data without any correlations between the FADC samples.
- The total dynamic range of the entire signal transmission chain was set to infinite, thus the detector has been simulated to be completely linear.
- The intrinsic arrival time spread of the photons was set to be 1 ns, as expected for γ -ray showers.
- Only one inner pixel has been simulated.

6.1 Bias

The signals were simulated with noise and extracted using the different extractor algorithms. For all sliding window algorithms the extraction window was allowed to move 5 FADC slices, independently of its size. For each signal extraction algorithm the average conversion factor between the reconstructed charge in FADC counts and the input number of photo-electrons was determined. The signal reconstruction bias was calculated as a function of the simulated number of photo-electrons N_{sim} :

$$B = \langle \widehat{N}_{\text{rec}} - N_{\text{sim}} \rangle \quad (10)$$

Figure 9 shows the results for some tested extractors, with different initializations. As expected, the fixed window extractor does not show any bias up to statistical precision. All other extractors however, do show a bias. Usually, the bias vanishes for signals above 5 photo-electrons, except for the sliding window. In this latter case, the bias only vanishes for signals above 12 photo-electrons. The best extractors have no bias above 3 photo-electrons and less than 1 photo-electron bias in the case of no signal ($N_{\text{sim}} = 0$).

6.2 Root Mean Square Error

In order to obtain the precision of a given extractor, we calculated the relative *RMSE*:

$$\text{Rel. } RMSE = \frac{1}{N_{\text{sim}}} \sqrt{\text{Var}[\widehat{N}_{\text{rec}}] + B^2} . \quad (11)$$

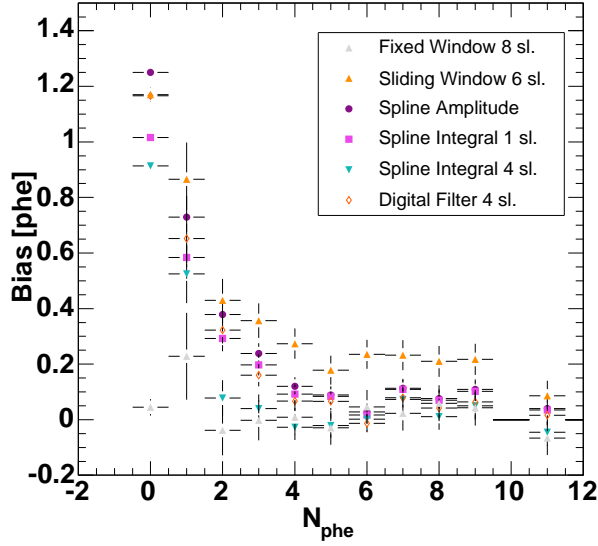


Fig. 9. Charge reconstruction bias as a function of the number of generated photo-electrons from MC simulations including electronic noise plus LONS. Above 12 photo-electrons, the bias vanishes for all signal extractors.

Figure 10 shows the relative $RMSE$ for the high gain and low gain parts separately. Also the square root of the relative variance of the number of simulated photo-electrons ($\sqrt{1/N_{sim}}$) is shown, which corresponds to the intrinsic fluctuations of the signal from air showers, following Poissonian statistics. Note, that the PMT introduces an additional excess noise [9], which is on average 1.18% of the Poissonian fluctuations for the MAGIC PMTs. For all extractors the variance of the reconstructed signal is dominated by noise and only slowly increases with rising signals due to mis-reconstruction of the signal pulse itself. Therefore, the relative $RMSE$ is proportional to $1/N_{phe}$. For small numbers of photo-electrons, extractors with small extraction windows or the digital filter yield the smallest values of $RMSE$, but the difference is only important below about 5 photo-electrons. Above that value, the curves for all extractors have crossed the black line, i.e. they are more precise than the intrinsic fluctuations of the signal. This is also true for the entire low gain extraction range.

The best results are obtained with the digital filter or a spline integrating 1 FADC slice. For the relatively narrow high gain pulse the spline amplitude yields comparable results, nevertheless for the wider low gain pulse the spline amplitude is subject to larger fluctuations and gives worse results compared to the digital filter and the spline integral.

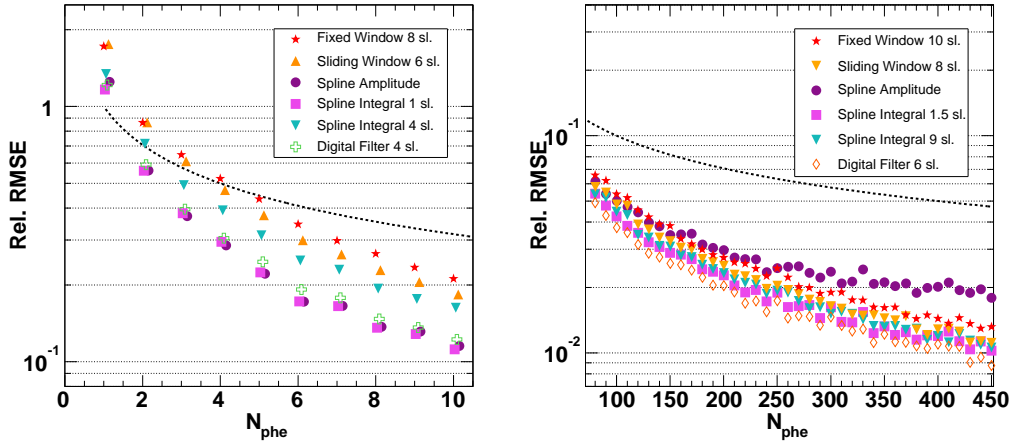


Fig. 10. Relative $RMSE$ as a function of the number of generated photo-electrons from MC simulations including fully simulated electronic noise plus LONS. Left: high gain, right: low gain. The black dashed line shows the square root of the relative variance of the incoming numbers of photo-electrons, note, that the PMT introduces an additional excess noise [9]. The best results are obtained with the digital filter or a spline integrating 1 FADC slice.

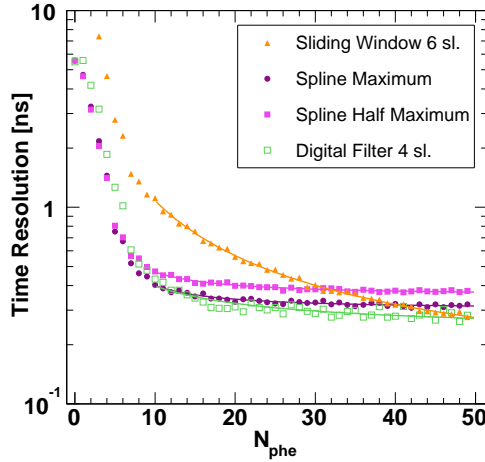


Fig. 11. Arrival time resolution as a function of the number of generated photo-electrons from MC simulations including fully simulated electronic noise plus LONS. For signals above 10 photo-electrons, all algorithms yield time resolutions better than 1 ns.

6.3 Arrival Times

Like in the case of the charge resolution, the time resolution Δt_{MC} of the reconstructed arrival time, t_{rec} , was calculated with respect to the simulated time t_{sim} :

$$\Delta t_{\text{MC}} \approx \text{RMS}(t_{\text{rec}} - t_{\text{sim}}) . \quad (12)$$

Figure 11 shows the arrival time resolution as a function of the simulated input signal charge and selected time extractor configuration. Above 10 photo-electrons, all algorithms yield time resolutions better than 1 ns, however the sliding window performs worse than the other algorithms since it does not use any shape information of the signal pulse. The average reconstructed arrival time is unbiased, i.e. it does not depend on the signal charge.

7 Pedestal Extraction

The pedestal is the average FADC count for the signal baseline (no input signal). To determine the pedestal setting off-line, dedicated pedestal runs are used, where the MAGIC read-out is randomly triggered. The fluctuations of the signal baseline are due to electronics noise as well as LONS fluctuations. Thus the pedestal RMS is a measure for the total noise level. It can be completely described by the noise-autocorrelation matrix \mathbf{B} , see equation (6). \mathbf{B} is independent of the signal extraction algorithm.

By applying the signal extractor to pedestal events, the bias B and the $RMSE$ for the case of no signal ($N_{\text{phe}} = 0$) can be determined. Table 1 shows the bias, the square root of the variance $\text{Var}[N_{\text{rec}}]$ and the root-mean-square error. In this sample, every extractor window had the freedom to move 5 FADC slices, i.e. the global window size was fixed to five plus the extractor window size.

One can see that the bias typically decreases and the variance increases with increasing sliding window size, except for the digital filter. The fixed window algorithm integrating eight FADC slices shows the worst $RMSE$ of 2.5 and 3 photo-electrons for an extra-galactic and a galactic star-field, respectively. Nevertheless, it has no bias. The extractor with the smallest $RMSE$ is the digital filter fitting 4 FADC slices with an $RMSE$ of 1.4 and 1.7 photo-electrons for an extra-galactic and a galactic star-field, respectively.

In the so-called image cleaning [8] only the camera pixels above a certain charge threshold are used for the image parameterization [7]. The charge threshold is adjusted such that the probability of being a noise fluctuation does not exceed a certain value. For the sake of comparison, a typical value of 3σ (0.3% probability) was chosen here and that number approximated with the formula:

$$N_{\text{phe}}^{\text{thres.}} \approx B + 3 \cdot \sqrt{V} . \quad (13)$$

$N_{\text{phe}}^{\text{thres.}}$ is shown in the 11th and 15th column of table 1. Again, most of the sliding window algorithms yield a smaller signal threshold than the fixed window, although the former ones have a bias.

The lowest threshold of only 4.2 photo-electrons for the extra-galactic star-field and 5.0 photo-electrons for the galactic star-field is obtained with the digital filter fitting 4 FADC slices. This is almost a factor 2 lower than the fixed window results. Also the spline integrating 1 FADC slice yields comparable results. In addition, table 1 shows the corresponding values from MC simulations. In the MC a slightly lower level of LONS has been simulated.

Name	Closed camera			MC simulation			Extra-galactic NSB				Galactic NSB			
	$\sqrt{\text{Var}[N_{rec}]}$	B	$RMSE$	$\sqrt{\text{Var}[N_{rec}]}$	B	$RMSE$	$\sqrt{\text{Var}[N_{rec}]}$	B	$RMSE$	$N_{phe}^{\text{thres.}}$	$\sqrt{\text{Var}[N_{rec}]}$	B	$RMSE$	$N_{phe}^{\text{thres.}}$
Fixed Win. 8	1.2	0.0	1.2	1.5	0.0	1.5	2.5	0.0	2.5	7.5	3.0	0.0	3.0	9.0
Slid. Win. 2	0.5	0.4	0.6	1.1	1.0	1.5	1.4	1.2	1.8	5.4	1.6	1.5	2.2	6.1
Slid. Win. 4	0.8	0.5	0.9	1.4	1.1	1.8	1.9	1.2	2.2	6.9	2.3	1.6	2.8	7.5
Slid. Win. 6	1.0	0.4	1.1	1.8	1.0	2.1	2.2	1.1	2.5	7.7	2.7	1.4	3.0	9.5
Slid. Win. 8	1.3	0.4	1.4	2.1	0.8	2.2	2.5	1.0	2.7	8.5	3.2	1.4	3.5	10.0
Spline Amp.	0.4	0.4	0.6	1.1	1.1	1.6	1.2	1.3	1.8	4.9	1.4	1.6	2.1	5.8
Spline Int. 1	0.4	0.3	0.5	1.1	0.8	1.4	1.2	1.0	1.6	4.6	1.3	1.3	1.8	5.2
Spline Int. 2	0.5	0.3	0.6	1.2	0.9	1.5	1.4	0.9	1.7	5.1	1.6	1.2	2.0	6.0
Spline Int. 4	0.7	0.2	0.7	1.3	0.8	1.5	1.7	0.8	1.9	5.3	2.0	1.0	2.2	7.0
Spline Int. 6	1.0	0.3	1.0	1.7	0.8	1.9	2.0	0.8	2.2	6.8	2.5	0.9	2.7	8.4
Dig. Filt. 4	0.4	0.3	0.5	1.0	1.3	1.6	1.1	0.9	1.4	4.2	1.3	1.1	1.7	5.0
Dig. Filt. 6	0.5	0.4	0.6	1.1	1.3	1.7	1.3	1.3	1.8	5.2	1.5	1.5	2.1	6.0

Table 1

The statistical parameters square root of reconstructed signal variance, bias, $RMSE$ and $N_{phe}^{\text{thres.}}$ for the tested signal extractors, applied to pedestal events. All units are in reconstructed numbers of photo-electrons, statistical uncertainty: about 0.1 photo-electrons. The extractors yielding the smallest values for each column are marked in red.

8 Calibration

In this section, tests are described which were performed using light pulses of different color, shape and intensity produced by the MAGIC LED calibration pulser system [19]. Such a system is able to provide fast light pulses of 2–4 ns FWHM with intensities ranging from 3 to more than 600 photo-electrons in one inner PMT of the MAGIC camera. These pulses can be produced in three colors, namely: **green**, **blue** and **UV**. Table 2 lists the available colors and intensities.

Color	Wavelength [nm]	Spectral Width [nm]	Min. No. Phe's	Max. No. Phe's	Secondary Pulses	FWHM Pulse [ns]
Green	520	40	6	120	yes	3–4
Blue	460	30	6	600	yes	3–4
UV	375	12	3	50	no	2–3

Table 2

The pulser colors available from the calibration system

Figure 12 shows examples of the smallest and largest intensity calibration pulses as recorded by the FADCs. Whereas the UV-pulse is very stable, the green and blue pulses can show smaller secondary pulses about 10–40 ns after the main pulse. One can see that the UV-pulses are only available in intensities which do not saturate the high gain read-out channel. However, the brightest combination of (blue) light pulses easily saturates all high gain channels of the camera, but does not saturate the low gain read-out.

The tests comprise three items:

- (1) Number of photo-electrons: The reconstructed number of photo-electrons should be independent of the signal extraction algorithm used.
- (2) Robustness tests: These tests investigate, for the different extractors, the stability of the reconstructed charges in FADC counts and number of photo-electrons (after calibration) in case of variations of the pulse form for the different extractors.
- (3) Time resolution: These tests show the time resolution for different intensities and colors.

8.1 Number of Photo-electrons

The mean number of photo-electrons $\langle \widehat{N}_{\text{phe}} \rangle$ was calculated for a sequence of calibration pulses of same intensity, following the excess noise factor method [9] and using different signal extractor algorithms. If the signals are extracted

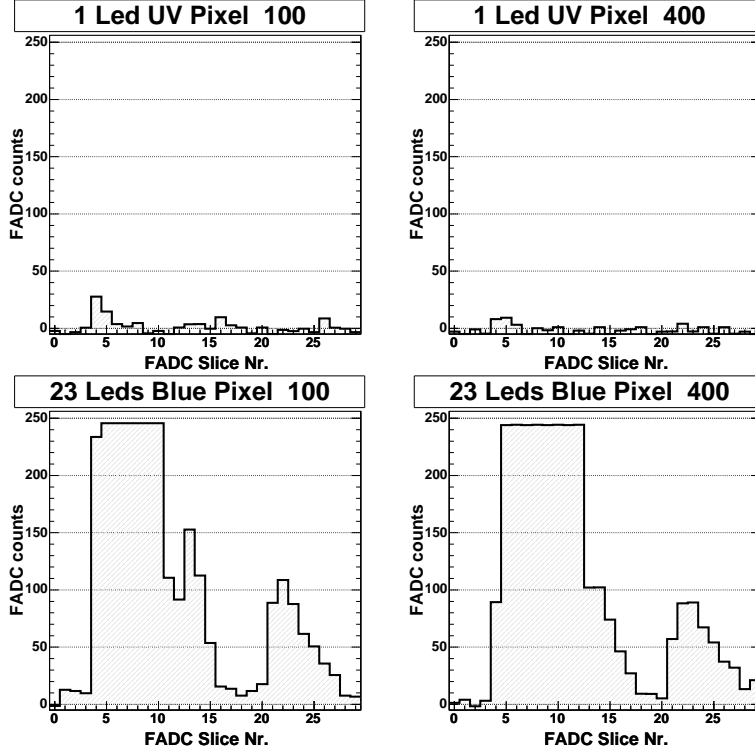


Fig. 12. Example of a calibration pulse from the lowest (top) and highest (bottom) available mono-chromatic intensity. Left: a typical inner pixel, right: a typical outer pixel. Note that in the upper plots, the pulse height fluctuates much more than suggested from these pictures. Especially, a zero-pulse is also possible. In the lower plots, the (saturated) high gain channel is visible at early times, while from FADC slice 20 on, the delayed low gain pulse appears.

correctly, $\langle \widehat{N}_{\text{phe}} \rangle$ should be independent of the signal extractor.

In our case, an additional complication arises from secondary pulses of the green and blue colored light pulses, which may introduce a dependence of $\langle \widehat{N}_{\text{phe}} \rangle$ on the extraction time-window size (recall figure 6). For the standard MAGIC calibration procedure [19] only UV calibration pulses are used.

Figure 13 shows $\langle \widehat{N}_{\text{phe}} \rangle$ for the standard UV calibration pulse. The results differ by less than 5%, which results in an additional systematic error to the reconstructed VHE γ -ray flux level, which is in total estimated to be 35% [3]. A small increase of $\langle \widehat{N}_{\text{phe}} \rangle$ for an increasing window size can be observed. This may be due to the intrinsic time structure of the calibration pulse.

The number of photo electrons has been reconstructed using the F-Factor method for various LED pulser intensities [19]. The peak-to-peak variation of the conversion factor between FADC counts and number of photo electrons for the different intensities is below 10% [27] for all extractors. The corresponding non-linearity is due to the intrinsic non-linearity of the MAGIC signal chain and a possible non-linear signal extraction.

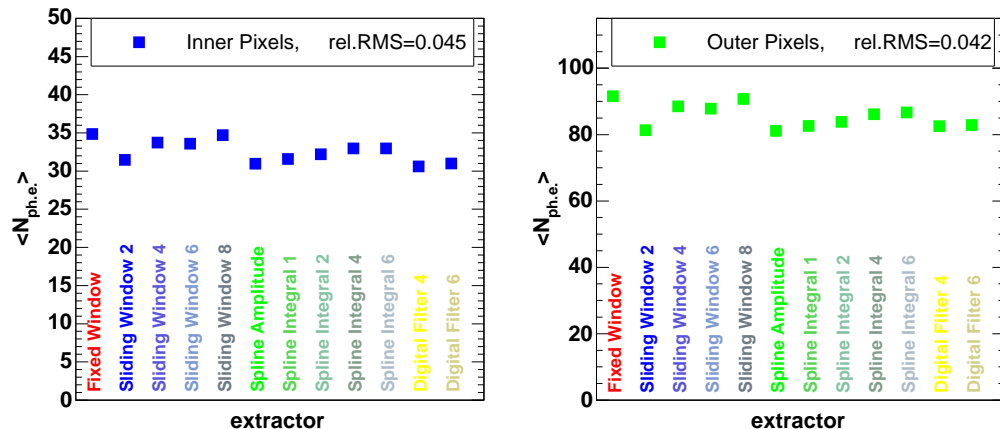


Fig. 13. $\langle \hat{N}_{\text{ph.e.}} \rangle$ from the standard calibration pulse, emitted by 10 UV LEDs, reconstructed with different signal extractors. Left: inner pixels, right: outer pixels. The statistical errors are smaller than the marker size.

8.2 Robustness Tests

Possible **variations of the pulse shape** may degrade the signal extraction quality of the MAGIC data. Variations of the pulse form have a physical reason: average Cherenkov pulses from hadronic showers are usually broader than those from electromagnetic ones. Additionally there are differences between the pulse form of calibration pulses and those of cosmic. These variations affect mainly those signal extractors which integrate part of a pulse or perform fits to a sample pulse form. In order to quantify the magnitude of the effect, table 3 lists the fraction of the pulse which is contained in typical time windows around the pulse maximum, for various pulse forms. While the amplitude extraction or integration of only 1 FADC slice around the maximum yield differences of as much as 10% (cosmic – UV), the error is reduced to about 3% if four FADC slices are getting integrated. Further deviations, characterized by the blue LED calibration pulse or the MC pulse, yield an even stronger discrepancy.

The digital filtering method assumes a constant signal shape to compute the weight functions. In fact, all pixels are assumed to have the same average signal shape and the same weights are used for all pixels. In order to test the robustness of the digital filtering method with respect to deviations of the actual pulse shape from the assumed pulse shape, the standard UV calibration pulse was extracted using different weight functions (computed for UV and blue calibration pulses, Cherenkov pulses and the low gain). The results are displayed in Figure 14 showing variations of about 8% in the reconstructed signal for typical pulse form variations and 3% in $\langle \hat{N}_{\text{ph.e.}} \rangle$ after calibration using the same weights file.

Window Size (FADC slices around maximum)	High Gain				Low Gain	
	MC	Cosmic	Calib. UV	Calib. Blue	Cosmic	Calib. Blue
	(percentage of complete pulse integral)					
Amplitude	5.4	5.0	4.5	4.1	3.4	2.5
1 slice	54	50	46	41	35	27
2 slices	78	76	71	66	60	48
4 slices	97	98	95	89	90	82

Table 3

Pulse form dependency of integration windows: Shown is the fraction of the signal (in percent of the complete pulse integral), contained in different time windows around the pulse maximum for different pulse shapes.

In conclusion, an event-to-event variation of the pulse shape may cause a charge reconstruction error of up to 10% for all signal extractors which do not integrate the whole pulse. The size of this error decreases with increasing integration window size. For the digital filter this event-to-event variation of the pulse shape may lead to an error of the reconstructed signal of up to 8%. A systematic difference in the pulse shape causes an error of up to 3% (after calibration) in the case of the digital filter.

8.3 Time Resolutions

The calibration light pulses can be used to test the time resolution of signal extractors. Thereby, the arrival time difference δt is measured for every channel, with respect to a reference channel:

$$\delta t_i = t_i - t_{\text{ref}} , \quad (14)$$

where t_i denotes the reconstructed arrival time of pixel number i and t_{ref} the reconstructed arrival time of the reference pixel. Using a calibration run of a fixed number of calibration pulses, the mean and RMS of the distribution of δt_i for a given pixel can be computed. The RMS is a measure of the combined time resolutions of pixel i and the reference pixel. Assuming that the photo-multipliers and read-out channels are of the same kind, an approximate time spread of pixel i is obtained as:

$$\Delta t_i \approx \text{RMS}(\delta t_i) / \sqrt{2} . \quad (15)$$

Figure 15 shows distributions of δt_i for an inner pixel obtained with four different arrival time extractors and two calibration pulses (the standard UV and

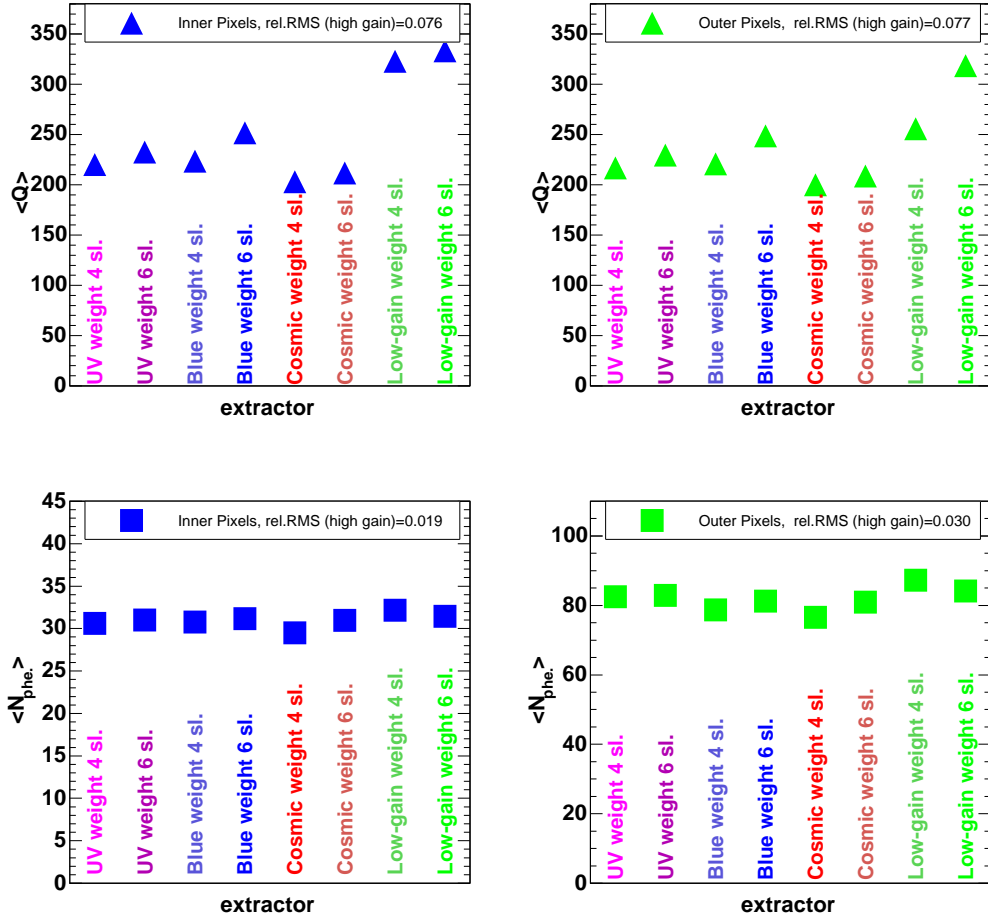


Fig. 14. Mean reconstructed charge in FADC counts (top) and $\langle \hat{N}_{\text{phe}} \rangle$ (bottom) from a standard calibration pulse reconstructed with a digital filter using different weight functions (computed for UV and blue calibration pulses, Cherenkov pulses and the low gain). Left: inner pixels, right: outer pixels. The relative RMS was calculated for the first six (high gain) pulse forms. The statistical errors are smaller than the marker size.

a high-intensity blue light). For the UV light pulses δt_i was determined in the high gain channel and for the strong blue pulses δt_i was determined in the low gain channel. In the high gain the mean and the variance of the δt_i are similar for the different extractors. All distributions but the one determined by the spline maximum position can be fitted well by Gaussians. In the low gain the digital filter and the half maximum position of the spline interpolation yield smaller variances compared to the sliding window and the spline maximum position. The average values of δt_i are similar, only the sliding window reconstructs a different value.

Figure 16 shows the obtained average time resolutions $\langle \Delta t_i \rangle$ as a function of $\langle \hat{N}_{\text{phe}} \rangle$ for various calibration runs taken with different colors and light

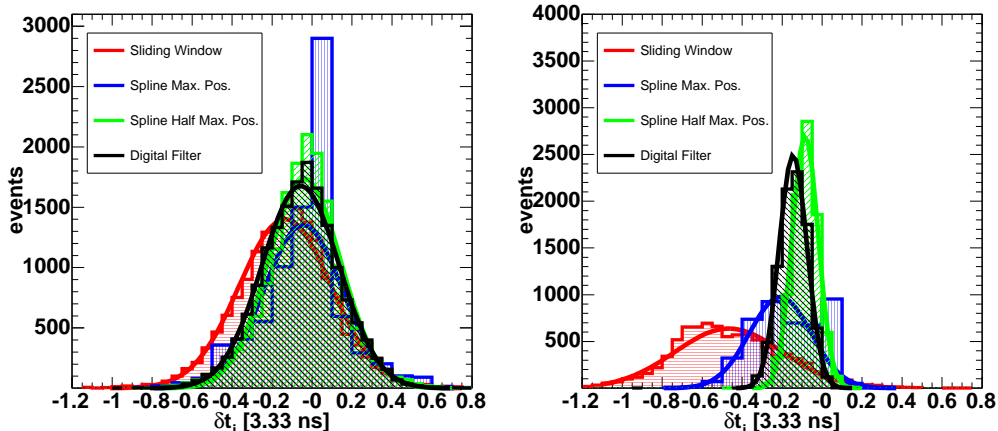


Fig. 15. Examples of distributions of arrival time differences (δt_i) for an inner pixel and the four arrival time extractors: Sliding Window with amplitude-weighted arrival time (red), maximum position of the interpolating spline (blue), half maximum position at rising edge of an interpolating spline (green) and the digital filter (black). The lines are Gaussian fits to the distributions. Left: medium sized UV pulse, extracted from the high gain channel, right: intense blue pulse, extracted from the low gain channel.

intensities and for three time extractors: a Sliding Window of 6 FADC slices with amplitude-weighted time, the Cubic Spline with the position of the half-maximum at the rising edge of the pulse as arrival time and the digital filter. One can see that the time spread decreases with increasing signal charge, as expected, and a time resolution of better than 1 ns can be obtained for all pulses above a threshold of 5 photo-electrons. For the largest signals, a time resolution of as good as 200 ps can be obtained. In order to understand the exact behavior of the time resolution, a short revision of its main contributions is listed here:

- (1) The intrinsic arrival time spread of the photons on the PMT: This time spread can be estimated roughly by the intrinsic width δt_{IN} of the input light pulse. The resulting time resolution is given by:

$$\Delta t \approx \frac{\delta t_{\text{IN}}}{\sqrt{N_{\text{phe}}}} . \quad (16)$$

The width δt_{IN} is about 1 ns for γ -ray pulses, a few ns for hadron pulses, for muons a few hundred ps and about 2–4 ns for the calibration pulses.

- (2) The transit time spread δt_{TTS} of the photo-multiplier (the spread of the times between the release of an electron from the photo cathode and the corresponding signal at the PMT output) which can be of the order of a few hundred ps per single photo electron, depending on the wavelength of the incident light. As in the case of the photon arrival time spread, the total time spread scales with the inverse of the square root of the number

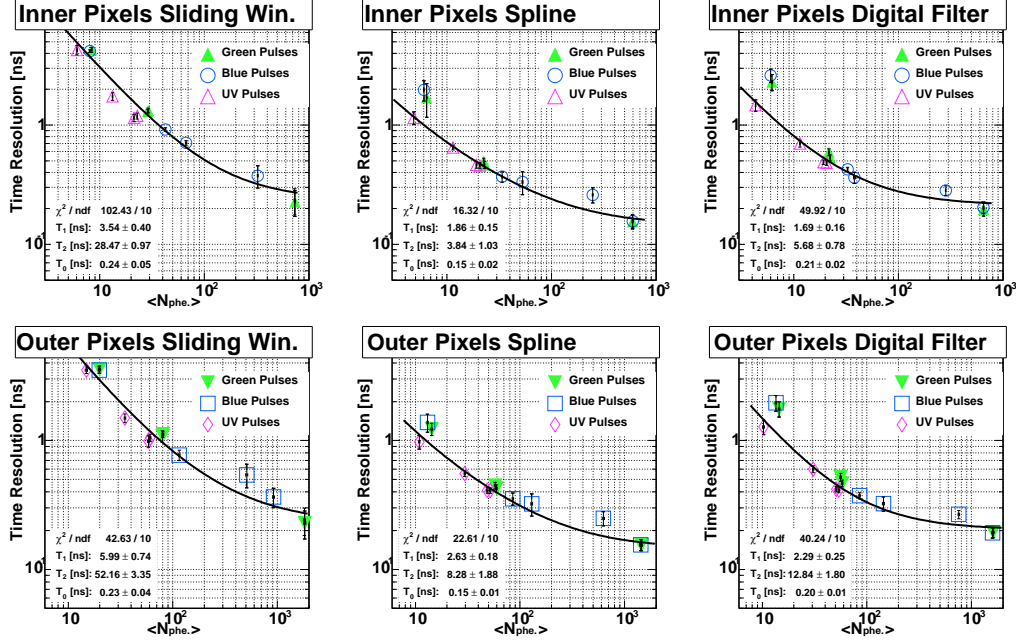


Fig. 16. Reconstructed mean arrival time resolution as a function of the extracted mean number of photo-electrons for different extractors, namely the amplitude weighted sliding window with a window size of 6 slices (left), the half-maximum searching spline (center), the digital filter with correct pulse weights over 6 slices (right). Error bars denote the spread (RMS) of time resolutions of the investigated channels. The marker colors show the applied pulser color, except for the last (green) point where all three colors were used. The lines are a fit using equation (20), see text for details. The best fit parameters are shown as an inset.

of photo-electrons:

$$\Delta t \approx \frac{\delta t_{\text{TTS}}}{\sqrt{N_{\text{phe}}}}. \quad (17)$$

- (3) The reconstruction error due to the background noise and limited extractor resolution:

$$\Delta t \approx \frac{\delta t_{\text{rec}} \cdot R / \text{phe}}{N_{\text{phe}}} \quad (18)$$

where $R = \sqrt{\text{Var}[\widehat{N}_{\text{phe}}]}$ is the square root of the extractor variance, defined in equation 3 which depends only very weakly on the signal charge.

- (4) A constant offset due to the residual FADC clock jitter or the MC simulation time steps.

$$\Delta t \approx \delta t_0. \quad (19)$$

In total, the time spread can be expressed as:

$$\Delta T = \sqrt{\frac{T_1^2}{N_{\text{phe}}} + \frac{T_2^2}{N_{\text{phe}}^2} + T_0^2}. \quad (20)$$

where T_1 contains the contributions of δt_{IN} and δt_{TTS} , the parameter T_2 contains the contribution of δt_{rec} and T_0 the offset δt_0 .

The measured time resolutions in figure 16 were fit by equation (20). The results of the fit are summarized in table 4. The low fit probabilities are partly due to the systematic differences in the intrinsic pulse shapes of the different color LED light pulses. Nevertheless, all calibration colors had to be included in the fit to cover the full intensity range. In general, the time resolutions for the UV pulses are systematically better than those for the other colors. This can be attributed to the fact that the UV pulses have a smaller intrinsic pulse width [27] – close to pulses from cosmic. There are clear differences between the studied time extractors, especially the sliding window extractor yields poorer resolutions. The spline and the digital filter are compatible within the errors. The parameters T_1 and T_0 should in principle be independent of the time extraction algorithm. Nevertheless, T_1 is larger for the sliding window algorithm than for the spline interpolation and the digital filter. This is in part due to the (anti)-correlation between the reconstructed charge and arrival time for the former extractor, see equation (5).

Signal Extractor	T_1	T_2	T_0	χ^2/NDF
Inner Pixels				
Sliding Window	3.5 ± 0.4	29 ± 1	0.24 ± 0.05	10.2
Spline Half Max.	1.9 ± 0.2	3.8 ± 1.0	0.15 ± 0.02	1.6
Digital Filter	1.7 ± 0.2	5.7 ± 0.8	0.21 ± 0.02	5.0
Outer Pixels				
Sliding Window	6.0 ± 0.7	52 ± 4	0.23 ± 0.04	4.3
Spline Half Max.	2.6 ± 0.2	8.3 ± 1.9	0.15 ± 0.01	2.3
Digital Filter	2.3 ± 0.3	13 ± 2	0.20 ± 0.01	4.0

Table 4

The results obtained from the fit of eq. 20 to the time resolutions obtained for various intensities and colors. The fit probabilities are very small mainly because of the different intrinsic arrival time spreads of the photon pulses from different colors.

Contrary to cosmic pulses, the calibration light pulses illuminate directly the camera, they are not reflected in the MAGIC mirror system. In order to get an upper limit for the reconstructed arrival time resolution of cosmic pulses, the effect of the mirrors has to be included. The MAGIC mirrors have been built in a parabolic shape, and are thus isochronous. Nevertheless, they have been staggered in a chess-board manner [28] with an offset of about 10 cm. This introduces an additional, binomial distributed contribution (about 700 ps width) to the intrinsic arrival times of the Cherenkov photons. Taking this effect into account, the expected time spread for inner pixels and cosmic pulses can be conservatively estimated to:

$$\Delta T_{\text{cosmic}} \approx \sqrt{\frac{4.5 \text{ ns}^2}{N_{\text{phe}}} + \frac{20 \text{ ns}^2}{N_{\text{phe}}^2} + 0.04 \text{ ns}^2}. \quad (21)$$

For signal charges above 10 photo-electrons the time resolution is below 830 ps. For signals of 100 photo-electrons the time resolution may be as good as 300 ps.

9 CPU Requirements

The speed of different extractor algorithms (the number of executed events per unit time) was measured on an Intel Pentium IV, 2.4 GHz CPU machine. Table 5 shows the average results whereby the individual measurements could easily differ by about 20% from one try to another (using the same extractor). The numbers in this list have to be compared with the event reading and decompression speed (400 evts/s). Every signal extractor being faster than this reference number does not limit the total event reconstruction speed. Only some of the integrating spline extractor configurations lie below this limit and would need to be optimized further.

Name	Events/sec. (CPU)
Fixed Window 14 slices	2700–3300
Sliding Window 6 slices	1000–1300
Spline Amplitude	700–1000
Spline Integral 1 sl.	300–500
Digital Filter	700–900

Table 5

The extraction speed measured for different signal extractor configurations. Note, that the fixed window does not calculate the arrival time.

10 Results and Discussion

Based on the previous investigations, the obtained results are summarized in table 6. The following criteria are used to compare the extractors:

- The extractor should yield on average the true number of photo-electrons and should not deviate by more than 10% in case of slight modifications of the pulse shape. This requirement excludes extractors which integrate only a small portion of the pulse, especially the amplitude sensing cubic spline extractor.

- The extractor must yield a stable low gain pulse extraction. This means that apart from being robust against modifications of the pulse shape, the extractor has to reconstruct on average the true signal charge also in case of variations of the pulse position within the recorded FADC samples. This criterion excludes the fixed window extractor since typical arrival time jitters are bigger than the time window between the tail of the high gain pulse and the beginning of the low gain pulse.
- The *RMSE* of the reconstructed charge for the case of no signal should not exceed 2 photo-electrons (an arbitrarily chosen threshold) for no-moon conditions and the *RMSE* of the reconstructed charge for air shower signals should never exceed the intrinsic Poissonian signal fluctuations plus excess noise above 5 photo-electrons. Camera pixels with a signal below 5 photo-electrons are usually rejected for the image parameterization [3, 7, 8]. This low-energy analysis condition discards the large sliding windows and the fixed window extractor. It is not critical for high-energy analyses, however.
- For analyses close to the energy threshold, an extractor should have a small or negligible bias, discarding again the amplitude sensing cubic spline extractor.
- The time resolution should not be worse than 2 ns at a signal strength of 10 photo-electrons (arbitrarily chosen threshold). Also this condition applies mostly to low-energy analyses where the arrival time information is needed to discriminate between signal and noise. All fixed window and all simple sliding window extractors are excluded by this condition.
- The needed CPU-time should not exceed the one required for reading the data into memory and writing it to disk. Unless further effort is made to speed up the integrating spline, it is excluded if used with a large integration window.

Table 6 shows which extractors fulfill the above criteria. One can see that there is no signal extractor without problems. However, the digital filter fitting four FADC slices can always be used for the high gain extraction, and the digital filter fitting six FADC slices for the low gain extraction. This combination has been chosen as the standard extractor for all MAGIC data. During a certain period, the pulse position was by mistake shifted with respect to the FADC read-out samples. In this case [29] the signal was reconstructed by the cubic spline algorithms integrating 1–2 FADC slices.

If efficiencies at low energies are not critical, i.e. a high analysis energy threshold without the use of the timing information, the sliding window extractor can be used in configurations which cover the entire pulse. This extractor turns out to be especially robust.

Extractor Configuration	robustness pulse form high gain	robustness pulse form low gain	$RMSE$	bias	time spread	Speed
Fixed Window 14 sl.	BEST	OK	NO	BEST	NO	BEST
Sliding Window 2 sl.	NO	NO	OK	OK	NO	OK
Sliding Window 4 sl.	OK	NO	NO	OK	NO	OK
Sliding Window 6 sl.	OK	OK	NO	OK	NO	OK
Sliding Window 8 sl.	OK	BEST	NO	OK	NO	OK
Spline Amplitude	NO	NO	OK	NO	OK	OK
Spline Integral 1 sl.	NO	NO	OK	OK	BEST	OK
Spline Integral 2 sl.	NO	NO	OK	OK	BEST	OK
Spline Integral 4 sl.	OK	NO	OK	OK	BEST	NO
Spline Integral 6 sl.	OK	OK	NO	OK	BEST	NO
Digital Filter 4 sl.	OK	NO	BEST	OK	OK	OK
Digital Filter 6 sl.	OK	OK	OK	OK	OK	OK

Table 6

The tested characteristics for every extractor. See text for descriptions of the individual columns. **OK** means, the extractor has passed the test, **NO** that the extractor failed and **BEST** that the extractor has succeeded a particular test as best of all.

11 Conclusions and Outlook

In this paper different algorithms to reconstruct the charge and arrival time from the FADC read-out samples of the MAGIC telescope have been developed. These algorithms are tested using MC simulations, pedestal and calibration events. The achievable charge and arrival time resolutions are determined. A digital filter fitting four FADC slices in the high gain channel and six FADC slices in the low gain was chosen as the standard signal extraction algorithm.

Part of the difficulties to find a suitable signal extractor (reflected in table 6) stem from the fact that the MAGIC signals are shaped just as long as to cover about four FADC slices. This choice, however necessary for a 300 MSamples/s FADC read-out, “washes out” the intrinsic pulse form differences between γ -ray and hadron showers, and prevents the analysis therefore from using this information in the γ /hadron discrimination. On the other side, the shaping time is not big enough to safely extract the amplitude of the (shaped) signal.

These problems will be overcome with the future installation of a 2 GHz FADC

system in MAGIC [14,15]. This system has been designed to reduce any pulse form deformation to the minimum. It can be expected that the individual pulse forms are then directly recognized as such, e.g. with a digital filter using two sample pulse forms (a γ -ray like and a hadron like) and discriminating between both with the help of the calculated χ^2 . These FADCs have a higher dynamic range and do not need a separate low gain channel any more. It can be expected that the signal extraction will become more robust, besides extracting a wealth of additional information about the shower characteristics.

A Acknowledgements

We would like to thank the IAC for the excellent working conditions at the Observatory de los Muchachos in La Palma. The support of the German BMBF and MPG, the Italian INFN and the Spanish CICYT is gratefully acknowledged. The MAGIC telescope is also supported by ETH Research Grant TH 34/04 3 and the Polish MNiI Grant 1P03D01028.

References

- [1] Baixeras, C. et al., 2004, Nucl. Instrum. Meth., A518, 188.
- [2] Albert, J. et al., 2006, ApJ, 637, L41.
- [3] Albert, J. et al., 2006, ApJ, 638, L101.
- [4] Lorenz, E. 2003, Nucl. Phys. B (Proc. Suppl.), 114, 217.
- [5] Albert, J. et al., 2005, Astroparticle Physics, 23, 493-509.
- [6] Mirzoyan, R. et al., 2006, Astropart. Phys., 25, 342.
- [7] Hillas, A. M., 1985, Proc. of the 19th ICRC, La Jolla, 3, 445.
- [8] Fegan, D. J., 1997, J. Phys. G., 23, 1013.
- [9] Mirzoyan, R. and Lorenz, E., 1997, Proc. of the 25th ICRC, Durban, South Africa, 7-265.
- [10] Bretz, T. and Wagner, R. (MAGIC Collab.), 2003, Proceedings of the 28th ICRC, Tsukuba, Japan, 2947.
- [11] Ostankov, A. et al., 2000, Nucl. Instrum. Meth., A442, 117.
- [12] Lorenz, E. et al., 2001, Nucl. Instrum. Meth., A461, 517.
- [13] Cortina, J. et al. (MAGIC Collab.), Prepared for International Symposium: The Universe Viewed in Gamma Rays, Kashiwa, Chiba, Japan, 25-28 Sep 2002.

- [14] Bartko, H. et al., 2005, Nucl. Instrum. Meth., A548, 464.
- [15] Paoletti, R. et al., 2006, to appear in IEEE Trans. Nucl. Sci..
- [16] Barrio, J. A. et al. (MAGIC Collab.), 1998, MPI-PhE 98-05.
- [17] Schweizer, T. et al., 2002, IEEE Trans. Nucl. Sci., 49, 2497.
- [18] Majumdar, P. et al. (MAGIC Collab.), 2005, Proc. of the 29th ICRC, Pune, India, 5-203, astro-ph/0508274.
- [19] Gaug, M. et al. (MAGIC Collab.), 2005, Proc. of the 29th ICRC, Pune, India, 5-375, astro-ph/0508274.
- [20] Chitnis, V. R. and Bhat, P. N., 2001, Astroparticle Physics, 15, 29.
- [21] James, F., Cousins, R. and Cowan, G., 2004, Review of Particle Physics, Phys. Lett., B592, 1, Chapter 32.
- [22] Press, W. H. et al., 2002, Cambridge University Press, second edition.
- [23] Cleland, W. E. and Stern, E. G., 1994, Nucl. Instrum. Meth., A338, 467.
- [24] Papoulis, A. 1977, McGraw-Hill.
- [25] Cojocary, C. et al., 2004, Nucl. Instrum. Meth., A531, 481.
- [26] Bartko, H. et al., Proc. 7th Workshop on Towards a Network of Atmospheric Cherenkov Detectors 2005, Palaiseau, France, 27-29 Apr 2005, astro-ph/0506459.
- [27] Gaug, M. 2006, PhD thesis, Universitat Autònoma de Barcelona, Barcelona, Spain, available at:
<http://wwwmagic.mppmu.mpg.de/publications/theses/MGaug.pdf>.
- [28] Garczarczyk, M., 2006, Ph.D. thesis, University of Rostock, to be published.
- [29] Albert, J. et al., 2006, ApJ, 642, L119.